PCCP

ROYAL SOCIETY OF CHEMISTRY

PAPER

Cite this: *Phys. Chem. Chem. Phys.*, 2022, **24**, 8166

Vibrational mode-specific dynamics of the $F^- + CH_3CH_2Cl$ multi-channel reaction†

Viktor Tajti and Gábor Czakó *

Received 10th February 2022,
Accepted 21st March 2022

DOI: 10.1039/d2cp00685e

rsc.li/pccp

We investigate the mode-specific dynamics of the ground-state, C–Cl stretching (ν_{10}), CH_2 wagging (ν_7), sym-CH_2 stretching (ν_1), and sym-CH_3 stretching (ν_3) excited $F^- + CH_3CH_2Cl(\nu_k = 0, 1)$ [k = 10, 7, 1, 3] → $Cl^- + CH_3CH_2F$ (S_N2), $HF + CH_3CHCl^-$, $FH\cdots Cl^- + C_2H_4$, and $Cl^- + HF + C_2H_4$ (E2) reactions using a full-dimensional high-level analytical global potential energy surface and the quasi-classical trajectory method. Excitation of the C–Cl stretching, CH_2 stretching, and CH_2/CH_3 stretching modes enhances the S_N2, proton abstraction, and $FH\cdots Cl^-$ and E2 channels, respectively. *Anti*-E2 dominates over *syn*-E2 (kinetic *anti*-E2 preference) and the thermodynamically-favored S_N2 (wider reactive *anti*-E2 attack angle range). The direct (a) S_N2, (b) proton abstraction, (c) $FH\cdots Cl^- + C_2H_4$, (d) *syn*-E2, and (e) *anti*-E2 channels proceed with (a) back-side/backward, (b) isotropic/forward, (c) side-on/forward, (d) front-side/forward, and (e) back-side/forward attack/scattering, respectively. The HF products are vibrationally cold, especially for proton abstraction, and their rotational excitation increases for proton abstraction, *anti*-E2, and *syn*-E2, in order. Product internal-energy and mode-specific vibrational distributions show that CH_3CH_2F is internally hot with significant C–F stretching and CH_2 wagging excitations, whereas C_2H_4 is colder. One-dimensional Gaussian binning technique is proved to solve the normal mode analysis failure caused by methyl internal rotation.

I. Introduction

Mode specificity has been widely studied for atom + molecule reactions,[1–23] however, the effect of vibrational excitations is less known for ion–molecule reactions,[24–37] such as the bimolecular nucleophilic substitution (S_N2). A typical S_N2 reaction in the gas phase has a submerged transition state as well as deep pre- and post-reaction minima supporting long-lived complex formations, which may undermine the mode-specific behavior. Nevertheless, a few early studies revealed non-statistical and mode-specific dynamics for S_N2 reactions,[24–29,38,39] however, these investigations only considered the $Cl^- + CH_3Y$ [Y = Cl and Br] systems using quasi-classical trajectory (QCT)[24] or 4-dimensional time-independent quantum methods[26–29] as well as kinetics[38] and spectroscopy[25,39] experiments. In the past decade the mode-specific dynamics of the $X^- + CH_3Y$ [X = F, Cl; Y = Cl, I] non-identity reactions were studied using high-level analytical potential energy surface (PES)-based QCT simulations[32,34,35] and time-dependent quantum computations.[30,31,33] Moreover, in 2018 Wester and co-workers reported the first direct measurement of the mode-specific dynamics of the $F^- + CH_3I$ S_N2 and proton-transfer reactions.[34] On one hand, these recent experimental and theoretical studies showed that CH stretching excitation has little effect on the S_N2 reactivity, whereas significantly enhances the proton-transfer channel.[34,35] On the other hand, CY stretching and umbrella-bending excitations promote the S_N2 reaction, showing that barrier-less complex-forming processes may also have mode-specific characters.[35]

All the previous mode-specific S_N2 studies focused on reactions of methyl–halides. Moving to more complex reactions of $X^- + CH_3CH_2Y$ introduces a new reaction channel *via* base-induced elimination (E2) leading to $Y^- + HX + C_2H_4$, besides the S_N2 pathways resulting in $Y^- + CH_3CH_2X$. Following a couple of pioneering electronic structure,[40–43] density functional theory-based direct dynamics,[44] and Car–Parrinello molecular dynamics[45,46] studies focusing on the $F^- + CH_3CH_2Y$ [Y = F, Cl, Br, I] reactions, in 2017 we reported a high-level *ab initio* characterization of the PES of the $F^- + CH_3CH_2Cl$ system considering S_N2 *via* Walden inversion, front-side attack, and double inversion as well as E2 and various high-energy product channels such as $HF + CH_3CHCl^-$, $FH\cdots Cl^- + C_2H_4$, $H^- + CH_3CHClF/CH_2FCH_2Cl$, and $FCl^- + CH_3CH_2$.[47] Utilizing the stationary-point information, we recently developed a full-

MTA-SZTE Lendület Computational Reaction Dynamics Research Group, Interdisciplinary Excellence Centre and Department of Physical Chemistry and Materials Science, Institute of Chemistry, University of Szeged, Rerrich Béla tér 1, Szeged H-6720, Hungary. E-mail: gczako@chem.u-szeged.hu

† Electronic supplementary information (ESI) available: Cross sections and reaction probabilities for double inversion, front-side attack, and induced inversion; Gaussian width test for 1GB; and mode-specific vibrational distributions for the CH_3CH_2F and C_2H_4 products obtained with histogram binning. See DOI: 10.1039/d2cp00685e

dimensional coupled-cluster-based analytical PES for the multi-channel $F^- + CH_3CH_2Cl$ reaction, allowing efficient QCT simulations and direct comparison with crossed-beam experiments.[48] Simulations played an essential role in distinguishing between the S_N2 and E2 channels, because the current experiments detected the ionic products, which is the same (Cl^-) for the two competing channels. We found that the E2 channel usually dominates over the thermodynamically favored S_N2 reaction, due to the wider range of the reactive attack angles for the former.[48]

In the present work, we investigate the mode-specific dynamics of the $F^- + CH_3CH_2Cl$ multi-channel reaction utilizing our recently-developed analytical PES[48] and the QCT method. The computations reveal the effect of initial mode-specific vibrational excitations on the reactivity and dynamics of the different reaction pathways and product channels. Besides the usual results of a standard QCT analysis, we report mode-specific polyatomic product-state distributions and utilize the energy-based Gaussian binning (1GB) technique,[49–51] for the first time, for an 8-atomic molecule (CH_3CH_2F). The computational details and methods are described in Section II, the results are presented and discussed in Section III, and the paper ends with summary and conclusion in Section IV.

II. Computational details

We perform QCT simulations for the $F^- + CH_3CH_2Cl$ reaction for the vibrational ground-state ($v = 0$), symmetric CH_2 ($v_1 = 1$) and CH_3 ($v_3 = 1$) as well as the C–Cl ($v_{10} = 1$) stretching-excited states, and the CH_2 wagging-excited ($v_7 = 1$) state of the polyatomic reactant (see Fig. 1) on a high-level *ab initio* full-dimensional analytical PES recently developed by the present authors[48] using the Robosurfer program system.[52] The initial vibrational states of CH_3CH_2Cl are prepared by standard normal mode sampling.[53] The rotational angular momentum of CH_3CH_2Cl is set to zero by modifying the initial velocities, and the relative orientation of the reactants is randomly sampled. We run QCTs at five different collision energies (8.1, 19.1, 26.5, 36.9, and 45.7 kcal mol^{-1}) and for five different vibrational states of CH_3CH_2Cl. The initial distance between the reactants is $\sqrt{x^2 + b^2}$, where x = 25 bohr, and the value of the b impact parameter (the distance between the velocity vectors of the reactants) is varied between zero and b_{max}, (where the reaction probability vanishes) with 0.5 bohr step size. Each trajectory is propagated until the longest atom-atom distance becomes larger by 1 bohr than the longest initial one. We run 1000 trajectories at each impact parameter – reactant excitation – collision energy combination; thus, this study is based on a total number of 595 000 trajectories.

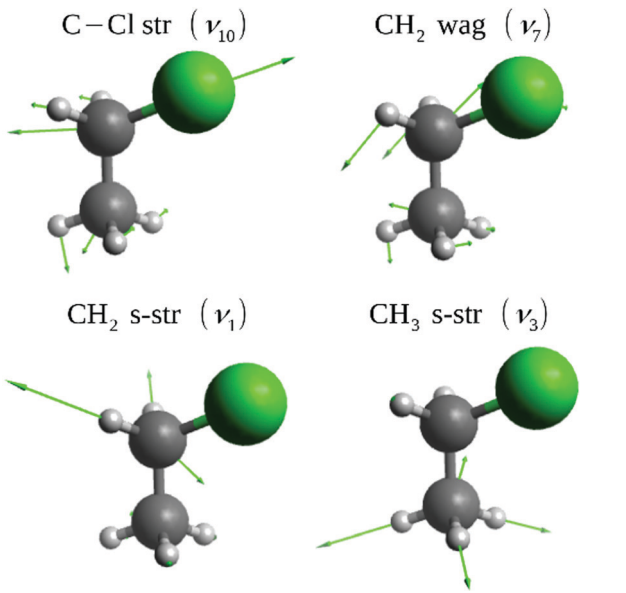

Fig. 1 Normal modes of CH_3CH_2Cl excited in the present dynamics simulations. The harmonic frequencies on the PES are ω_{10} = 697, ω_7 = 1330, ω_1 = 3104, and ω_3 = 3048 cm^{-1}.

Integral cross sections (ICSs) are calculated using a b-weighted numerical integration of the $P(b)$ opacity functions (the P reaction probabilities as a function of b). Differential cross sections are obtained using standard histogram binning (HB). We apply different zero-point energy (ZPE) restrictions for the ICSs: (1) soft: the sum of the classical vibrational energies of the products must be larger than the sum of the harmonic ZPEs of the polyatomic products and, in the case of the proton-transfer channel and the two E2 channels, the sum of the classical internal energy of HF and the vibrational energy of the polyatomic product must be larger than sum of the anharmonic ZPE of the diatomic HF molecule corresponding to its given rotational state and the harmonic ZPE of the polyatomic product. The variationally-determined anharmonic rovibrational levels of the HF molecule are taken from ref. 54. (2) hard: the previous constraints are set separately for each product and we exclude trajectories from the reactive ones if any condition does not hold. We apply no ZPE-constraints to differential cross sections.

We distinguish between the retained or inverted configuration of the polyatomic product for the S_N2 channel by using a vector-projection scheme, which was introduced in ref. 55. First we define a Cartesian coordinate system with the alpha-carbon (CH_2–carbon) atom at the origin and calculate the cross product of the position vectors of the beta-carbon (CH_3–carbon) atom and the halogen atom. Then, we evaluate the dot product of the obtained normal vector and the difference of the position vectors of the two hydrogen atoms bound to alpha carbon. Dot-product values are determined in the case of the initial (CH_3CH_2Cl) and final (CH_3CH_2F) geometries of the reactive S_N2 trajectories, and we compare the signs of the dot products: the same and opposite signs refer to retention and inversion, respectively.

To distinguish between the front-side-attack (FS S_N2) and double-inversion[56] (DI S_N2) pathways, we scan the trajectories in a backward direction until we reach a transition state (TS) defined by the C–Cl distance becoming less than 4.0 bohr (2.1 Å) as the C–Cl distances at the front-side attack and Walden-inversion TSs are 2.362 and 2.197 Å on the PES, respectively. At this TS geometry, we separate the front-side attack TS from the Walden-inversion TS (second TS of the DI

S_N2 pathway) by applying a limit of 111° (based on ref. 55 and 57) to the F–C–Cl attack angle (γ). Thus, γ less than 111° is a sign of front-side attack, whereas γ greater than 111° refers to the double-inversion mechanism.

In case of the two types of E2 trajectories, *syn* and *anti*, we find the TS region at 3.8 bohr C–Cl distance following the E2 trajectories backwards similarly to the above-described retention case. At the TS geometry we calculate the cosine of the Cl–C_α–C_β–F dihedral angle and if its value is positive (negative), then the trajectory is assigned to the *syn*- (*anti*-) pathway. We note that the present reaction channel and pathway assignment is not exactly the same as the one used in ref. 48, which results in somewhat different numerical results, especially for the minor $FH\cdots Cl^-$ complex forming and *syn*-E2 channels, but this does not affect any conclusions.

We determine the mode-specific vibrational energies of the polyatomic products based on the procedure described in detail in ref. 51. First, we perform normal-mode analysis for the optimized products to obtain their harmonic vibrational frequencies (ω_k) and normal-mode eigenvectors. Then, we remove the angular momentum of the products by modifying velocities. In the next step, we use an Eckart-transformation,[51,58] also taking H-atom permutations into account, to find the best overlap[59] between the optimized/reference and the actual/final structure. Then, we transform the mass-scaled Cartesian displacement coordinates and velocities by using the eigenvectors obtained in the first step to determine the normal coordinates (Q_k) and momenta (P_k). Finally, we determine the mode-specific harmonic vibrational energies (E_k) and the integer vibrational quantum numbers (n_k), in atomic units, as

$$E_k = P_k^2/2 + (\omega_k Q_k)^2/2, \quad (1)$$

$$n_k = \lfloor E_k/\omega_k \rfloor, \quad (2)$$

where the floor sign $\lfloor\ \rfloor$ refers to rounding down to an integer value and $k = 1, \ldots, 3N-6$, where N is 8 and 6 for CH_3CH_2F and C_2H_4, respectively. For the diatomic HF product, rotational and vibrational quantum numbers are assigned as detailed in ref. 54.

Vibrational distributions are obtained by histogram binning and in the case of the CH_3CH_2F products one-dimensional Gaussian binning (1GB)[49–51] is also employed. For 1GB we use the GB(harm-exact) approach, as proposed in ref. 51, which defines a Gaussian weight for each product as

$$G_p(\mathbf{n}) = \frac{\beta}{\sqrt{\pi}} e^{-\beta^2\left(\frac{E(\mathbf{n}'_p)-E(\mathbf{n})}{2E(\mathbf{0})}\right)^2} \quad p = 1, 2, \ldots, N(\mathbf{n}), \quad (3)$$

where $\mathbf{n} = (n_1, n_2, \ldots, n_{3N-6})$, $\beta = 2\sqrt{\ln 2}/\delta$, δ is the full-width at half-maximum, $E(\mathbf{n}'_p)$ is the exact classical vibrational energy of the pth product obtained by using the final Cartesian coordinates and velocities, $E(\mathbf{n})$ is the harmonic vibrational energy obtained by the quantum mechanical energy expression of a harmonic oscillator, and $E(\mathbf{0})$ is the harmonic ZPE. In the present 1GB analysis for the mode-specific vibrational distributions of the CH_3CH_2F products, δ is set to 0.2, after testing different values between 0.1 and 1.0.

III. Results and discussion

A. Reaction pathways

The different reaction pathways and their energetics of the F^- + CH_3CH_2Cl S_N2 and E2 reactions are shown in Fig. 2. The S_N2 channel is highly exothermic and its energetically favored Walden-inversion (or back-side attack, bs) pathway proceeds *via* a pre-reaction complex (Premin C_s), a submerged Walden-inversion transition state (W TS), and a post-reaction minimum (S_N2 postmin) leading to the Cl^- + CH_3CH_2F products. Furthermore, the S_N2 reaction has two retention pathways: double inversion[56] begins with a proton abstraction induced inversion *via* DI TS, followed by a second inversion *via* W TS, whereas front-side attack goes over a high-energy FS TS as Fig. 2 shows. In the case of the inversion *via* DI TS, it is also possible that this first inversion is not followed by a reactive substitution event and an inverted reactant molecule is formed. We call this process as induced inversion.[56] Beside the S_N2 channel, the title reaction can produce Cl^- + HF + C_2H_4 products *via* elimination, which is also exothermic, but thermodynamically less favored. The E2 reaction can proceed with *anti*- and *syn*-E2 mechanisms *via* the submerged *Anti*-E2 and *Syn*-E2 TSs (see Fig. 2), where the simultaneously leaving FH and Cl^- groups are in *anti* and *syn* arrangements, respectively. Energetically the *anti*-E2 pathway is preferred, as the *Anti*-E2 TS is below *Syn*-E2 TS by about 10 kcal mol^{-1}, whereas *Anti*-E2 and W TSs have the same energy within 1 kcal mol^{-1}; thus, one may expect high competition between the *anti*-E2 and S_N2 channels. It is also important to note that the *syn*-E2 pathway goes through $FH\cdots Cl^-$ + C_2H_4, which is the most exothermic product channel of the title reaction below the S_N2 and E2 products by about 11 and 23 kcal mol^{-1}, respectively. Of course, upon dissociation of the $FH\cdots Cl^-$ complex, this channel may also lead to E2 products. Besides the exothermic pathways, proton abstraction from the alpha carbon atom may produce HF + CH_3CHCl^- products *via* an endothermic process. Note that proton abstraction from the beta carbon leads to E2 breakup, thus HF + $CH_2CH_2Cl^-$ products are not expected ($CH_2CH_2Cl^-$ does not exist in a stable form). Fig. 2 also shows the comparison of relative energies of the stationary points along the different reaction pathways obtained on the analytical PES[48] with all-electron CCSD(T)/complete-basis-set-quality benchmark data.[47,60] As seen, the PES values usually agree with the benchmark data within 0.5 kcal mol^{-1} confirming the high-accuracy of the full-dimensional analytical PES.

B. Intramolecular vibrational-energy redistribution

One of the main concerns about mode specificity in polyatomic reaction dynamics is the intramolecular vibrational-energy redistribution (IVR) prior to collision. In order to investigate IVR in CH_3CH_2Cl, we follow the ground-state and vibrationally-excited reactant in time without interaction with F^- and compute the mode-specific vibrational energies as shown in Fig. 3. As seen, IVR does occur even in the first picosecond, the low frequency modes gain energy on the expense of the high-energy ones; nevertheless, some mode specificity is maintained even after 6 ps. In the case of the CH stretching excited modes the energy loss is fast and these mode energies approach the energies of the non-excited CH stretching modes in the first few

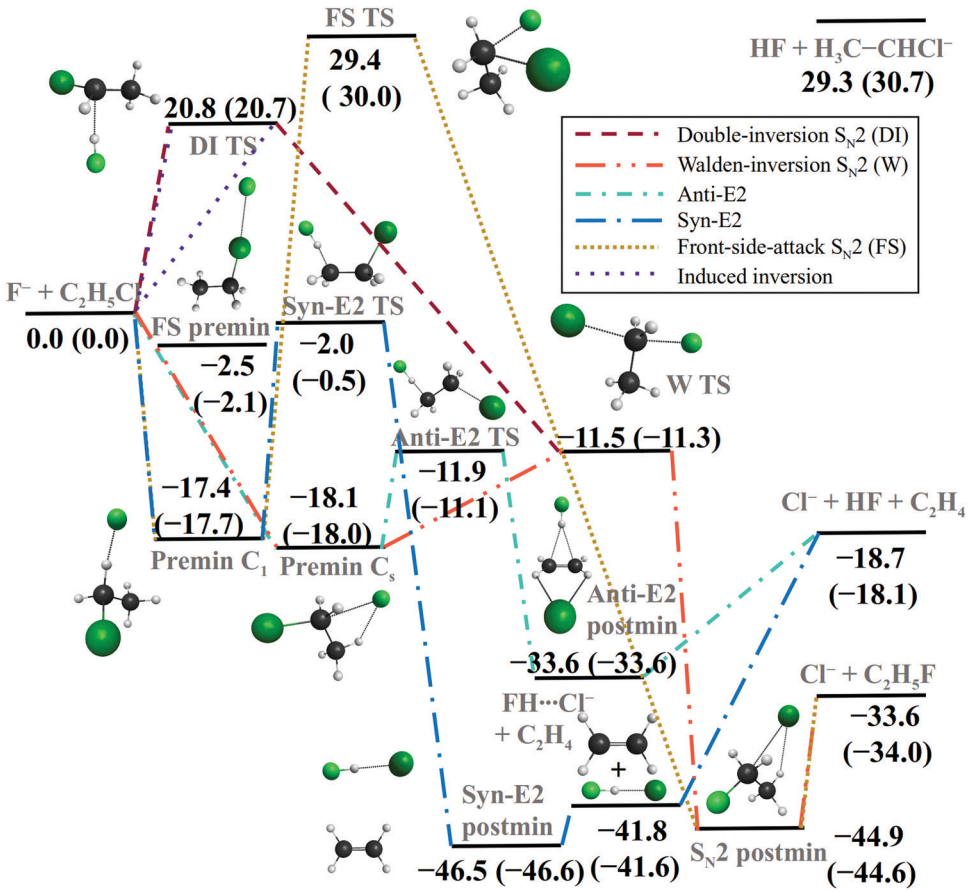

Fig. 2 Schematic potential energy surface of the $F^- + CH_3CH_2Cl$ reaction showing the classical relative energies (in kcal mol^{-1}) of the stationary points along the different reactions pathways corresponding to the fitted PES[48] and (benchmark CCSD(T)-F12b/aug-cc-pVQZ + Δ_{core}[CCSD(T)-F12b/cc-pCVTZ-F12] level of theory).[47,60]

hundred femtoseconds. Thus, IVR may partially undermine mode specificity in the title reaction, nevertheless, some effects may be expected as the mode energies remain non-statistical during the timeframe of collision in the present simulations. Regarding the mode-specific normal mode analysis, we must highlight a technical issue related to the fast unphysical increase of the symmetric CH_3 stretching mode energy after 1 ps. This is due to the failure of the rectilinear normal coordinates and the harmonic approximation at highly distorted geometries; occurring, in the present case, at eclipsed conformations resulting in large displacement coordinates for the beta H atoms relative to the staggered reference structure. This issue does not cause problem in the kinetic energy part, but unphysically increases the harmonic potential part and thus the total vibrational symmetric CH_3 stretching mode energy as seen in Fig. 3. Nevertheless, it is important to note that this technical issue of the normal mode analysis does not affect the QCT computations, because the trajectories are propagated in the Cartesian space using the fully-anharmonic PES.

C. Separation of the different reaction pathways

Before we present the QCT results, let us discuss the separation of the different reaction pathways leading to the same products. In the case of the double-inversion and front-side attack S_N2 retention pathways the transition-state-attack-angle-based approach was discussed in detail in ref. 55 and 57; thus, in the present article we focus on the E2 mechanisms. Fig. 4 shows the Cl–C_α–C_β–F transition-state dihedral angle distributions for the E2 trajectories. At the lowest collision energy, the distribution peaks at 180°, decreases with decreasing angle, and virtually vanishes around 90°, showing the dominance of the *anti*-E2 pathway. As the collision energy increases a second peak emerges around 30° as a signature of the *syn*-E2 mechanism. At higher collision energies the *syn*-E2 probability becomes significant, but *anti*-E2 remains the dominant E2 pathway. As Fig. 4 shows at all collision energies the two peaks around small and large angles are clearly distinct and the probabilities around 90° are close to zero; thus, the *syn*- and *anti*-E2 pathways can be almost unambiguously separated using a dividing limit of 90° for the Cl–C_α–C_β–F transition-state dihedral angle. This is comforting, because visual analysis of tenths of thousands of E2 trajectories considered in the present study would be highly exhaustive and undesired.

D. Mode-specific reactivity

Mode-specific cross sections as a function of collision energy for the S_N2 inversion, proton-abstraction, $FH\cdots Cl^-$ complex formation, and *syn*/*anti*-E2 channels are given in Fig. 5. The S_N2

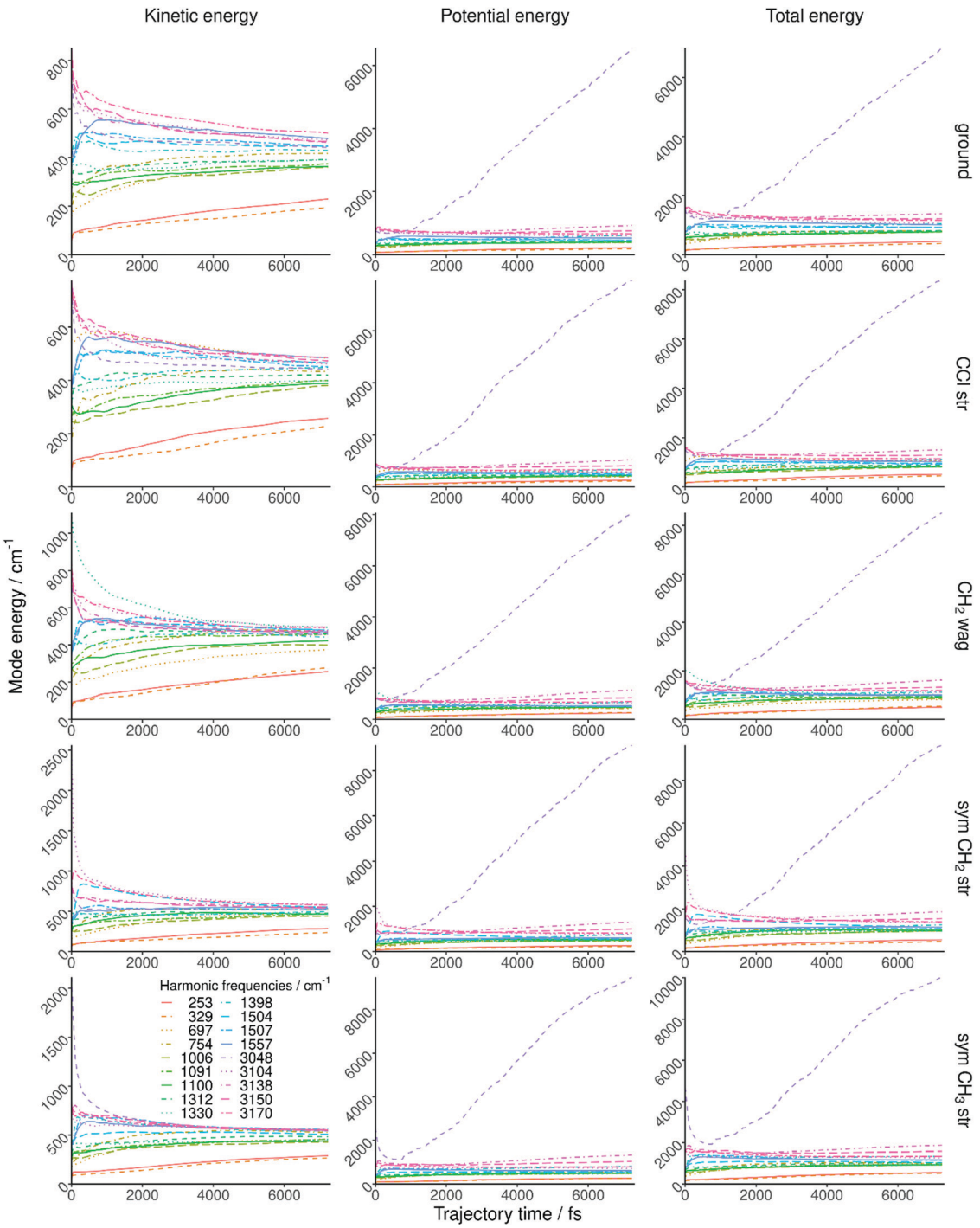

Fig. 3 Mode specific vibrational energies and their kinetic and potential energy parts of the $CH_3CH_2Cl(v_k = 0, 1)$ [k = 10, 7, 1, 3] molecules as a function of time (t) averaged over 100 trajectories and time from 0 to t. The potential and total energies for the symmetric CH_3 stretching mode (ω_3 = 3048 cm^{-1}) are unphysical (see text for details).

cross sections are large and decrease with increasing collision energy as expected for a barrier-less (W TS is below the reactants) exothermic reaction. C–Cl stretching excitation clearly enhances the S_N2 reactivity by 20, 36, 48, 54, and 47% at collision energies of 8.1, 19.1, 26.5, 36.9, and 45.7 kcal mol^{-1}, respectively, whereas the effects of the other modes are less significant. The ZPE-constrained cross sections are virtually the same as the non-constrained ones, due to the fact that the CH_3CH_2F products are usually internally hot. Note that in the case of the S_N2 channel the soft and hard constraints are exactly the same, because there is only one multi-atomic product.

The reactivity of proton abstraction increases with increasing collision energy and for this channel significant mode specificity is seen. Reactant vibrational excitation enhances

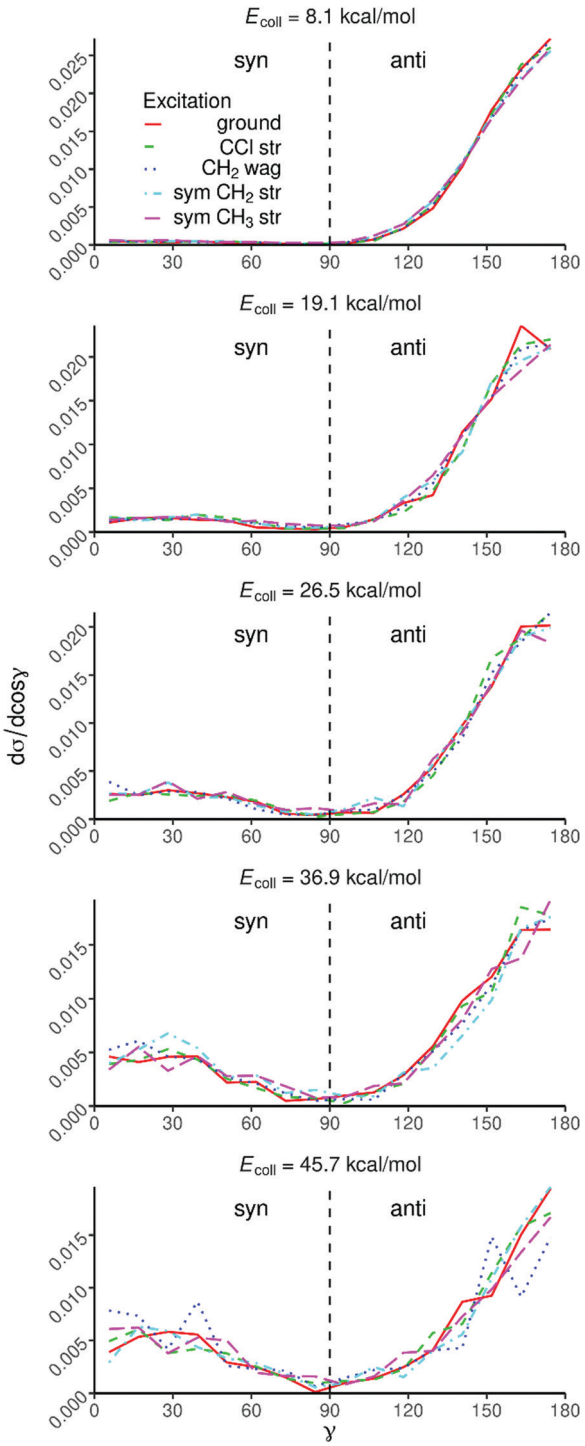

Fig. 4 Distributions of the Cl–C_α–C_β–F dihedral angles at the E2 transition states for the $F^- + CH_3CH_2Cl(v_k = 0, 1) \rightarrow Cl^- + HF + C_2H_4$ [k = 10, 7, 1, 3] reactions at different collision energies.

the reactivity, and the most substantial effect is found for the CH_2 stretching, as expected, because the proton is abstracted from the CH_2 group. ZPE constraints significantly reduce the abstraction reactivity and shifts the threshold energy toward larger values, in agreement with the endothermicity. These results clearly show that most of the proton-abstraction products violate ZPE, and with hard constraint only the CH_2 stretching excited reaction provides considerable reactivity at high collision energy.

The cross sections for the $FH\cdots Cl^-$ + C_2H_4 and *syn*-E2 channels show similar dependence on collision energy and initial vibrational excitation as expected, because both pathways go through the same *Syn*-E2 TS. In both cases the reactivity decreases with increasing collision energy and CH_2 and CH_3 stretching excitations enhance the reaction the most efficiently. On one hand, this effect of the CH_3 stretching mode is expected, because in both cases a proton is abstracted from the beta carbon atom. On the other hand, the enhancement upon CH_2 stretching excitation is due to IVR between these modes. Considering the magnitude of the CH_2/CH_3 vibrational enhancement factors, we find more substantial enhancement by a factor of 2–4, especially with ZPE constraints, for the *syn*-E2 channel, than in the case of the $FH\cdots Cl^-$ channel. This may be explained by the fact that vibrational excitation facilitates the dissociation of the $FH\cdots Cl^-$ complex, thereby enhancing the *syn*-E2 channel. ZPE constraints reduce the reactivity for the *syn*-E2 channel, nevertheless, the shapes of the excitations functions are not significantly affected. For the highly-exothermic $FH\cdots Cl^-$ channel, ZPE violation is negligible.

The *anti*-E2 channel dominates the title reaction, this pathway is strongly favored over *syn*-E2, as expected since the *Anti*-E2 TS is well below the *Syn*-E2 TS and the *Anti*-E2 postmin is less deep than the *Syn*-E2 postmin (see Fig. 2). Furthermore, the *anti*-E2 reactivity is even larger than that of the S_N2 channel, especially at low collision energies and usually expect in the hard constrained case. This finding is somewhat unexpected, because the S_N2 reaction is thermodynamically preferred and kinetic control also does not explain this substantial reactivity difference, because the *Anti*-E2 and W TSs are nearly isoenergetic. The reason must be in the different dynamics of the two channels,[48] which will be revealed and discussed later. Similar to the *syn*-E2 channel, CH_2/CH_3 stretching excitations enhance the *anti*-E2 channel the most efficiently, especially when ZPE constraints are applied and ZPE constraints decrease the reactivity. The constraints, especially the hard one, have more substantial effects on the less exothermic E2 channel than in the case of the S_N2 reaction where ZPE violation is negligible, this is why the E2/S_N2 reactivity ratio changes when hard constraint is applied. Furthermore, we note that ZPE constraints may artificially enhance the mode-specific effects on the E2 channel as less product ZPE violation is expected if the reactant is vibrationally excited.

Cross sections (Fig. S1, ESI†) and reaction probabilities (Fig. S2, ESI†) for the front-side attack, double-inversion, and induced-inversion pathways are shown in the ESI.† Retention and induced-inversion reactivity is small, around 0.1% as Fig. S2 (ESI†) shows, and we only find retention trajectories for the initially excited reactions. Front-side attack opens above 30 kcal mol^{-1} as expected based on its barrier height (29.4 kcal mol^{-1}). Double inversion dominates at lower collision energies (20–40 kcal mol^{-1}) and it is the most efficiently enhanced by CH_2 stretching excitation, because the first inversion begins with a proton abstraction from the alpha carbon atom. We also

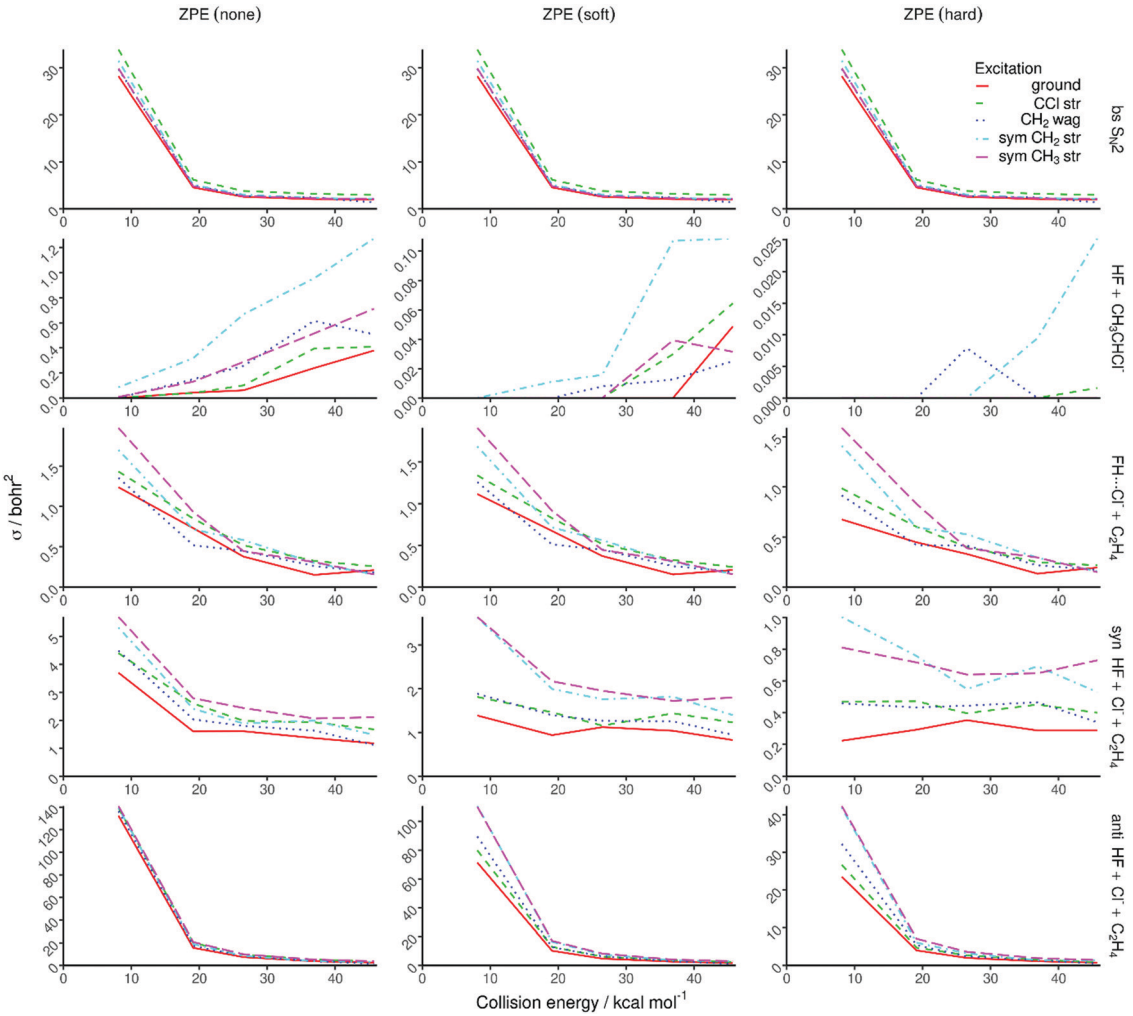

Fig. 5 Cross sections for the different product channels or pathways of the $F^- + CH_3CH_2Cl(v_k = 0, 1)$ [k = 10, 7, 1, 3] reactions as a function of collision energy obtained without and with soft and hard ZPE constraints.

find induced-inversion trajectories in similar collision energy range and with similar reactivity as double inversion, though for induced inversion one reactant ground-state trajectory is also found at collision energy of 19.1 kcal mol^{-1}. In the case of the retention and induced-inversion pathways the CH_3CH_2F and the inverted-CH_3CH_2Cl molecules are formed internally hot; thus, the soft and hard constraints do not affect the cross sections as seen in Fig. S1 (ESI†), in accord with our previous findings for the $F^- + CH_3Br$ reaction.[57] Furthermore, we note that for the F^- + methyl–halide systems the retention and induced-inversion reactivity is significantly larger than in the present case,[55,57] indicating that the CH_3 ligand hinders these channels.

E. Opacity functions and angular distributions

Opacity functions, scattering angle distributions, and initial attack angle distributions at different collision energies are shown in Fig. 6, 7, and 8, respectively. For the S_N2 channel the reaction probabilities decrease with increasing impact parameter and collision energy, and the b_{max} values also decrease with increasing collision energy from about 15 bohr at 8.1 kcal mol^{-1} and reaching a nearly constant value of ~6 bohr at 26.5 kcal mol^{-1}. The corresponding scattering angle distributions are backward–forward symmetric at the lowest collision energy and become backward dominant at higher collision energies, in accord with the smaller b_{max} values favoring backward scattering. The attack angle distributions are almost isotropic at the lowest collision energy with only slight back-side attack preference, whereas as the collision energy increases the back-side attack dominance becomes more and more significant. At the highest collision energy of 45.7 kcal mol^{-1} basically no reactivity is seen from the front-side (Cl-side) attack hemisphere (0–90°). These findings indicate that the S_N2 reaction is indirect at low collision energies and becomes direct rebound dominated favoring back-side attack and backward scattering as the collision energy increases, in accord with the textbook picture of Walden inversion. The increase of the S_N2 reactivity upon C–Cl stretching excitation is clearly seen in Fig. 6, but the shapes of the opacity functions and the different angle distributions do not change within statistical accuracy.

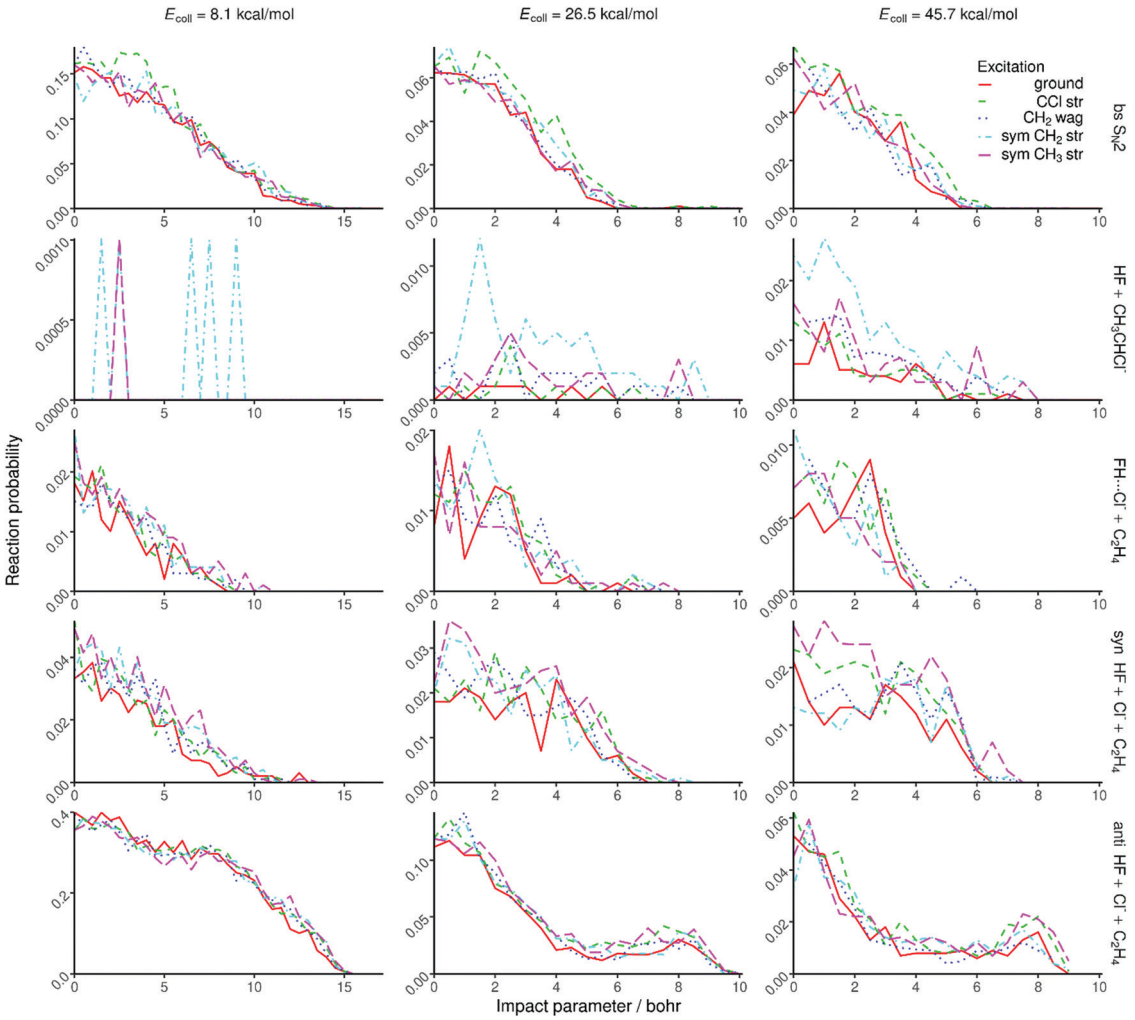

Fig. 6 Reaction probabilities for the different product channels or pathways of the F^- + $CH_3CH_2Cl(v_k = 0, 1)$ [k = 10, 7, 1, 3] reactions as a function of impact parameter at different collision energies obtained without ZPE constraint.

The proton-abstraction channel of the ground-state reaction has small reactivity, usually below 1% even at the highest collision energy considered in the present study. Upon vibrational excitation of the reactant, especially for the CH_2 stretching, the reaction probabilities as well as the b_{max} values significantly increase as seen in Fig. 6. The scattering angle distributions show forward scattered dominance indicating significant stripping mechanism. The attack angle distributions are somewhat isotropic with large statistical uncertainty due to the small reactivity, which hinders any conclusion about the mode-specific effects on the abstraction mechanism.

On one hand, the decaying opacity functions and the nearly isotropic angle distributions of the $FH\cdots Cl^-$ + C_2H_4 and *syn*-E2 channels are similar at the lowest collision energy, indicating indirect pathways in both cases. On the other hand, as the collision energy increases and the reactions become more direct, interesting differences emerge between the two channels, which are the most pronounced at the highest collision energy. While both channels are mainly forward scattered, the b_{max} values become much smaller for the $FH\cdots Cl^-$ formation. Considering the attack angle distributions, the side-on collisions (relative to the C–Cl bond) favor the $FH\cdots Cl^-$ formation, whereas clear front-side attack preference is seen for the *syn*-E2 channel. These findings show the different direct pathways of the two channels. In the case of *syn*-E2, F^- comes parallel with the C–Cl bond from the Cl-side, abstracts the proton, and Cl^- leaves forward while HF moves into somewhat opposite direction, without the possibility of $FH\cdots Cl^-$ complex formation. $FH\cdots Cl^-$ formation can occur when F^- approaches from the CH_3 group perpendicular to the C-Cl bond, abstracts the proton, and the HF fragment moves toward the leaving Cl^- and the forming $FH\cdots Cl^-$ complex scatters forward considering the path of the Cl ligand.

In the case of the *anti*-E2 channel the b_{max} values are larger than those of *syn*-E2 and S_N2, especially at higher collision energies in the latter case. At high collision energies the opacity functions show a small peak at large impact parameters as a signature of direct striping mechanism. At the lowest collision energy, the *anti*-E2 scattering angle distributions are backward–forward symmetric indicating indirect dynamics, and as the collision energy increases and the reaction becomes more direct,

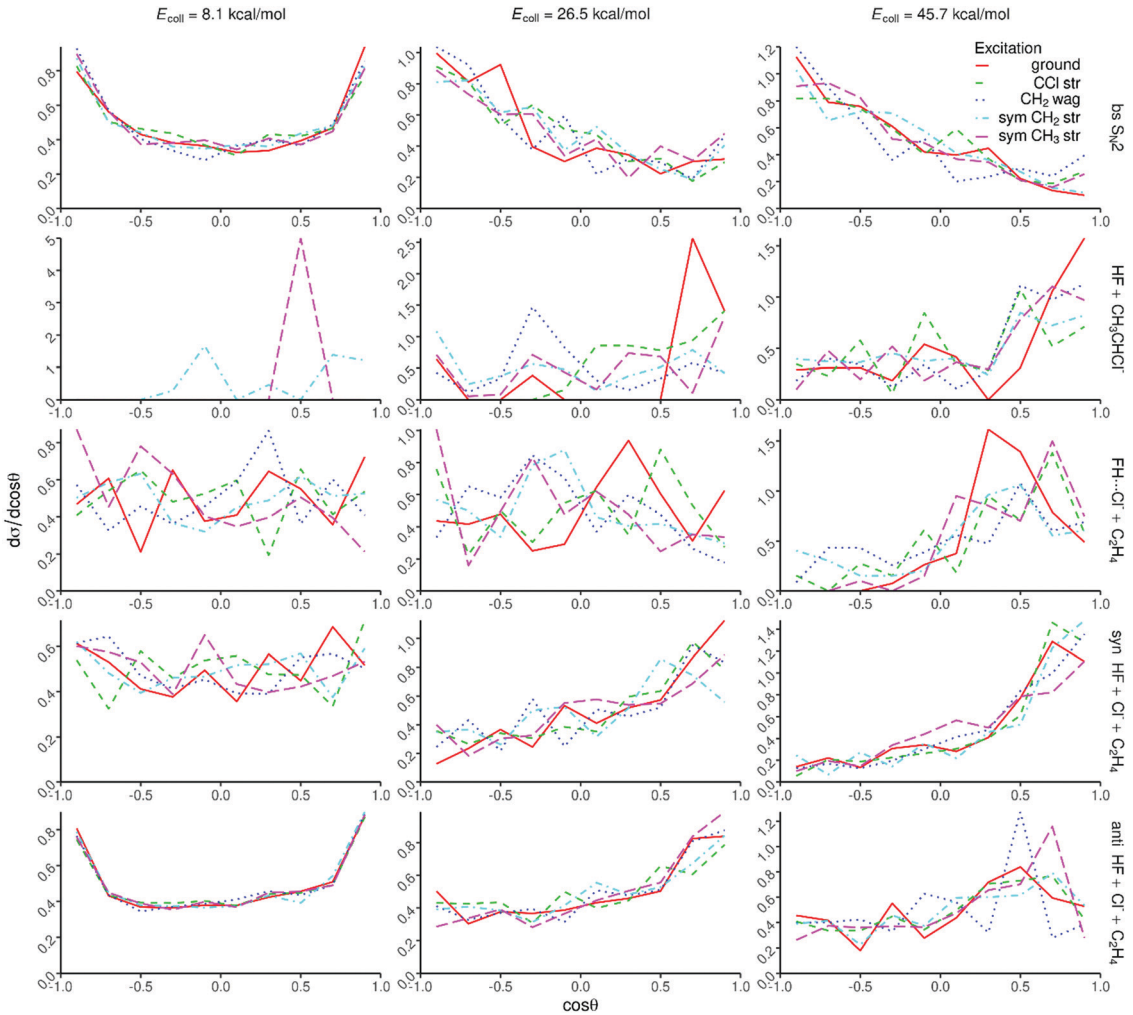

Fig. 7 Scattering angle distributions for the different product channels or pathways of the F^- + CH_3CH_2Cl(v_k = 0, 1) [k = 10, 7, 1, 3] reactions at different collision energies. The scattering angle is defined as the supplement of the angle between the velocity vector of F^- and the (center of mass) velocity vector of Cl^- or (CH_3CHCl^- or $FH\cdots Cl^-$).

the forward scattering dominates. This finding indicates that F^- usually strips the proton from the CH_3 group while the leaving Cl^- moves forward without significantly changing its direction. The *anti*-E2 attack angle distributions nearly mirror the corresponding *syn*-E2 ones, *i.e.*, back-side attack favors the *anti*-E2 pathway, especially at higher collision energies, as expected looking at the structure of the *Anti*-E2 TS. At this point we can explain the larger reactivity of the E2 pathway compared to S_N2. As seen in Fig. 6, the opacity functions of the *anti*-E2 pathway show higher preference of large impact parameters than the S_N2 channel, and at higher collision energies, the reactive attack angle range is much wider for the E2 pathways than in the case of S_N2 as seen in Fig. 8. For the $FH\cdots Cl^-$ and E2 channels one can see the initial vibrational excitation effects on the reaction probabilities; however, the changes in the shapes of the opacity functions and angle distributions are not significant at the given level of statistics.

F. Internal energy distributions

Internal energy distributions of the products of the different reaction channels or pathways are shown in Fig. 9 and 10. Fig. 9 shows that the CH_3CH_2F product of the S_N2 channel is formed internally highly excited. The CH_3CH_2F distributions become blue-shifted, broader, and their peaks shift toward lower energies indicating the dominance of direct dynamics as collision energy increases. Initial CH_2/CH_3 stretching excitations blue-shift the product internal energies, showing that these high-frequency "spectator" modes usually remain excited in the S_N2 product as well. For the C–Cl stretching mode the effects on the product internal energies are less significant due to the stronger coupling of this mode with the reaction coordinate.

As Fig. 9 also shows, the proton-abstraction channel forms cold HF molecules; their internal energy distributions peak at the lowest energies showing significant ZPE violation, especially at low collision energies. The CH_3CHCl^- co-product is more excited, but significant ZPE violation is also seen. Here mode-specific effects cannot be assessed due to the low statistical accuracy of this minor channel.

The $FH\cdots Cl^-$ complex and the C_2H_4 co-product have Gaussian-like, rather hot internal energy distributions with negligible ZPE violation. The $FH\cdots Cl^-$ distributions peak

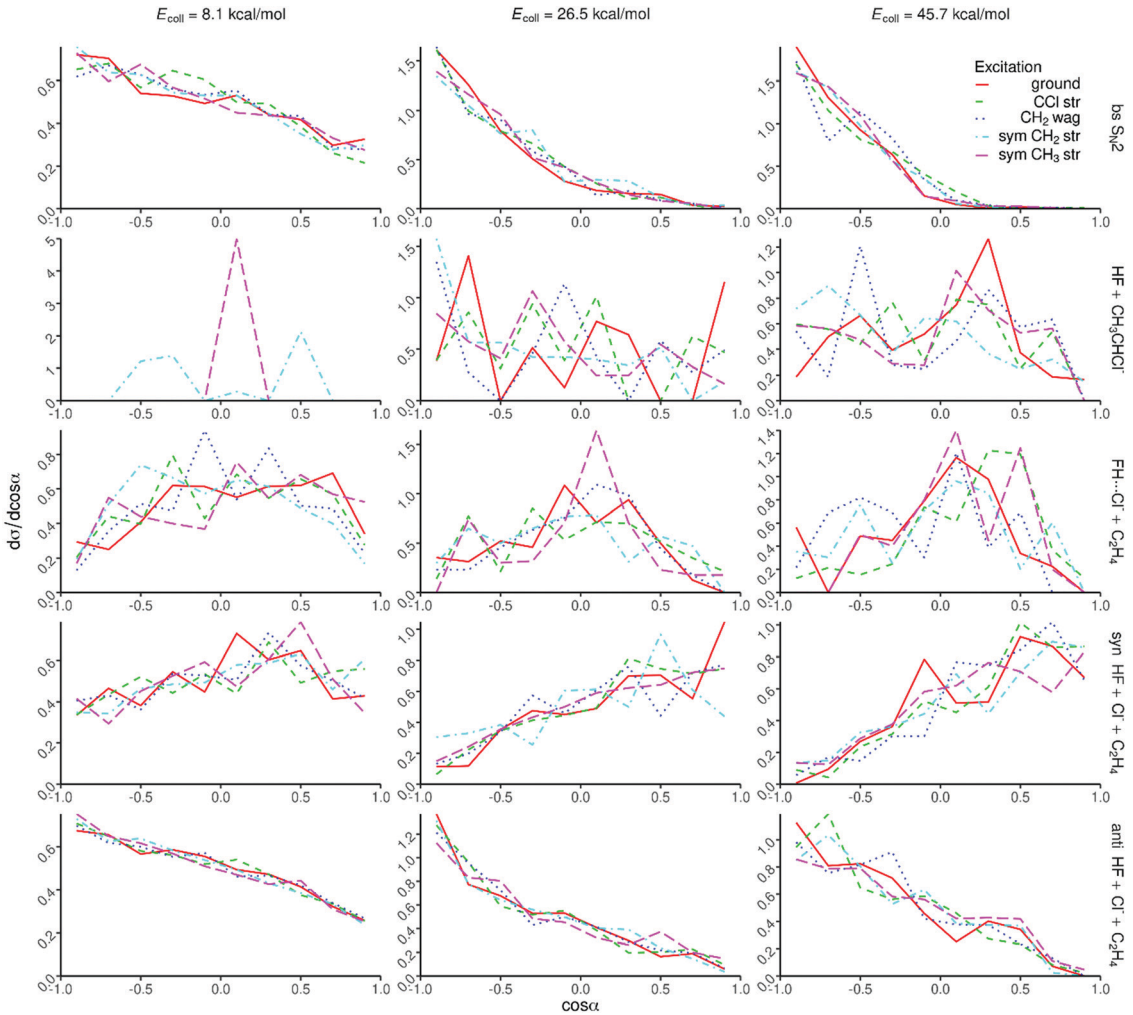

Fig. 8 Initial attack angle distributions for the different product channels or pathways of the F^- + $CH_3CH_2Cl(v_k = 0, 1)$ [k = 10, 7, 1, 3] reactions at different collision energies. The attack angle is defined as the angle between the velocity vector of the center of mass of CH_3CH_2Cl and the vector from C_α to Cl at time zero.

around the D_e value (23.1 kcal mol^{-1}) of the complex, thus, significant fraction of the products has larger internal energy than the dissociation energy; thus, this complex exists in a Feshbach-type resonance[61] state. The initial vibrational energy transfers rather into the C_2H_4 fragment as the blue-shifted distributions show in Fig. 9. We may also assume that in the case of significant vibrational energy transfer into the $FH\cdots Cl^-$ fragment, the complex dissociates and E2 products are formed.

The internal energy distributions for the *syn*- and *anti*-E2 products are shown in Fig. 10. Significant differences between the product distributions obtained for the two pathways are not found. In both cases the HF molecules are internally cold, their internal energy distributions peak at zero energy showing substantial ZPE violation, in accord with the ZPE-constrained cross sections shown in Fig. 5. Note that the HF molecules formed by the proton-abstraction channel are even more colder, as expected, because proton abstraction is an endothermic, whereas E2 is an exothermic process. The C_2H_4 E2 co-products are internally hot with only little ZPE violation, except for the ground-state reaction at low collision energies. As collision energy increases a tail emerges in the C_2H_4 distributions at higher internal energies, which is the best seen for the *anti*-E2 channel. Initial vibrational energy mainly transfers into the C_2H_4 product, though some shifts toward higher energies are also seen for HF as well.

G. HF vibrational and rotational distributions

Quantum-state-resolved vibrational distributions for the HF products of the proton-abstraction, *syn*-E2, and *anti*-E2 channels are shown in Fig. 11. In the case of the proton-abstraction channel, the HF product molecules are almost always in vibrational ground state, only a few % $v = 1$ population is seen at the highest collision energy. For the E2 pathways the HF products are slightly more excited, but the ground-state HF is still the dominant (80–90%). The population of the $v = 1$ state is 10–20%, and a few % probability is found for $v = 2$. The excitation of HF often increases by only 1–2% upon initial vibrational excitation and/or the increase of the collision energy. The HF vibrational populations do not show any significant dependence on the *syn*- and *anti*-mechanism of the E2 channel. These findings are in agreement with the HF internal energy distributions shown in Fig. 9 and 10.

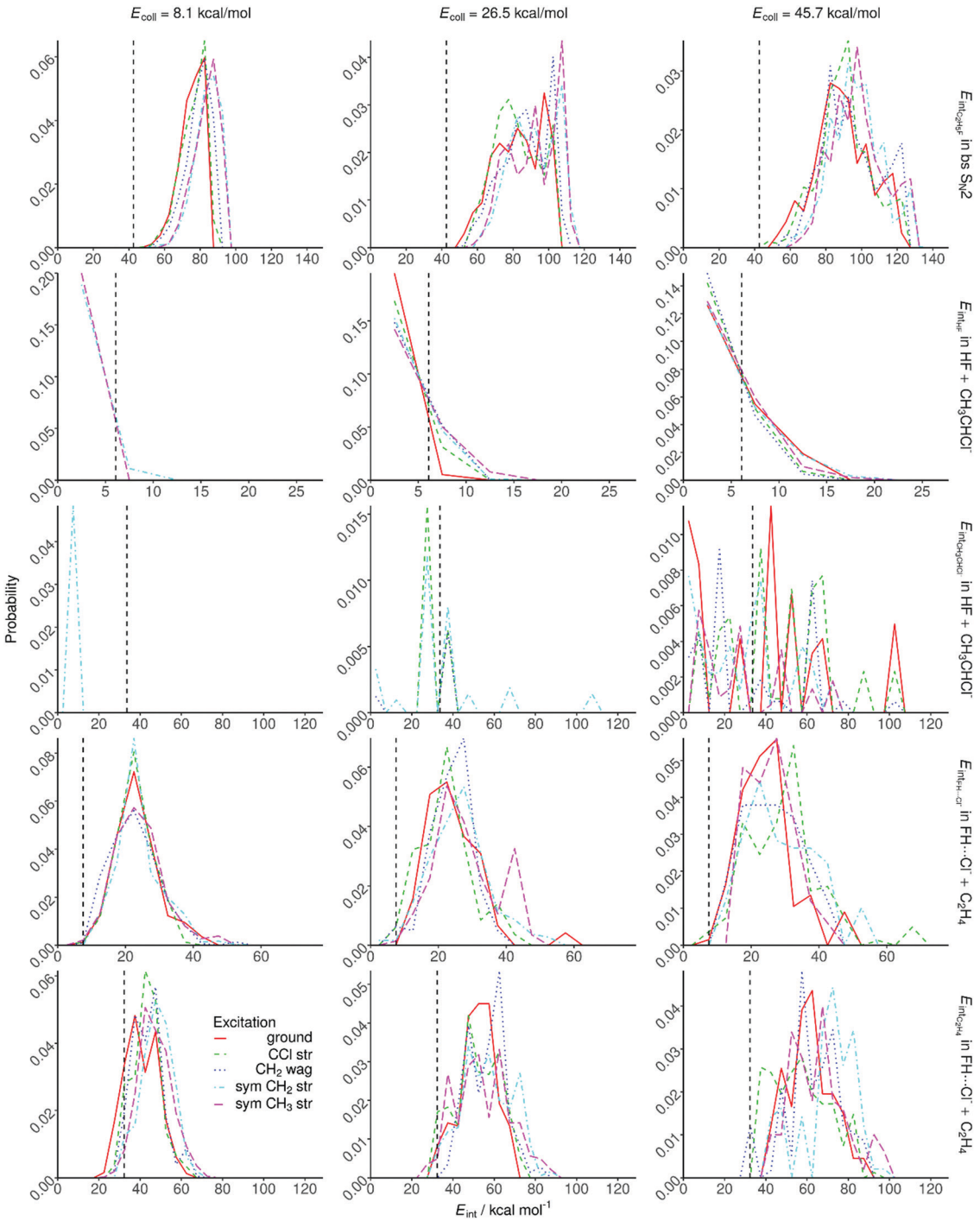

Fig. 9 Normalized product internal energy distributions for the F^- + $CH_3CH_2Cl(v_k$ = 0, 1) [k = 10, 7, 1, 3] → Cl^- + CH_3CH_2F, HF + CH_3CHCl^-, and $FH\cdots Cl^-$ + C_2H_4 reactions at different collision energies. Vertical dashed lines indicate the ZPE of the products.

The HF rotational distributions for the above-discussed channels are shown in Fig. 12. The HF molecules formed by proton abstraction are rotationally cold; the rotational distributions usually peak at J = 1–2. Some initial translational and vibrational energy transfer into HF rotation are seen, but this finding is not significant at the given level of statistics. The HF products of the E2 channel are rotationally hotter, and unlike for the vibrational distributions, here significant *syn*/*anti* mechanism dependence is found, *i.e.*, the *syn*-E2 HF products are rotationally more excited than the *anti*-E2 ones. Collision energy transfer into HF product rotation is seen, whereas the vibrational energy transfer is not significant.

H. Mode-specific vibrational distributions for polyatomic products

We have also computed mode-specific vibrational distributions for the polyatomic product (CH_3CH_2F) of the S_N2 channel as

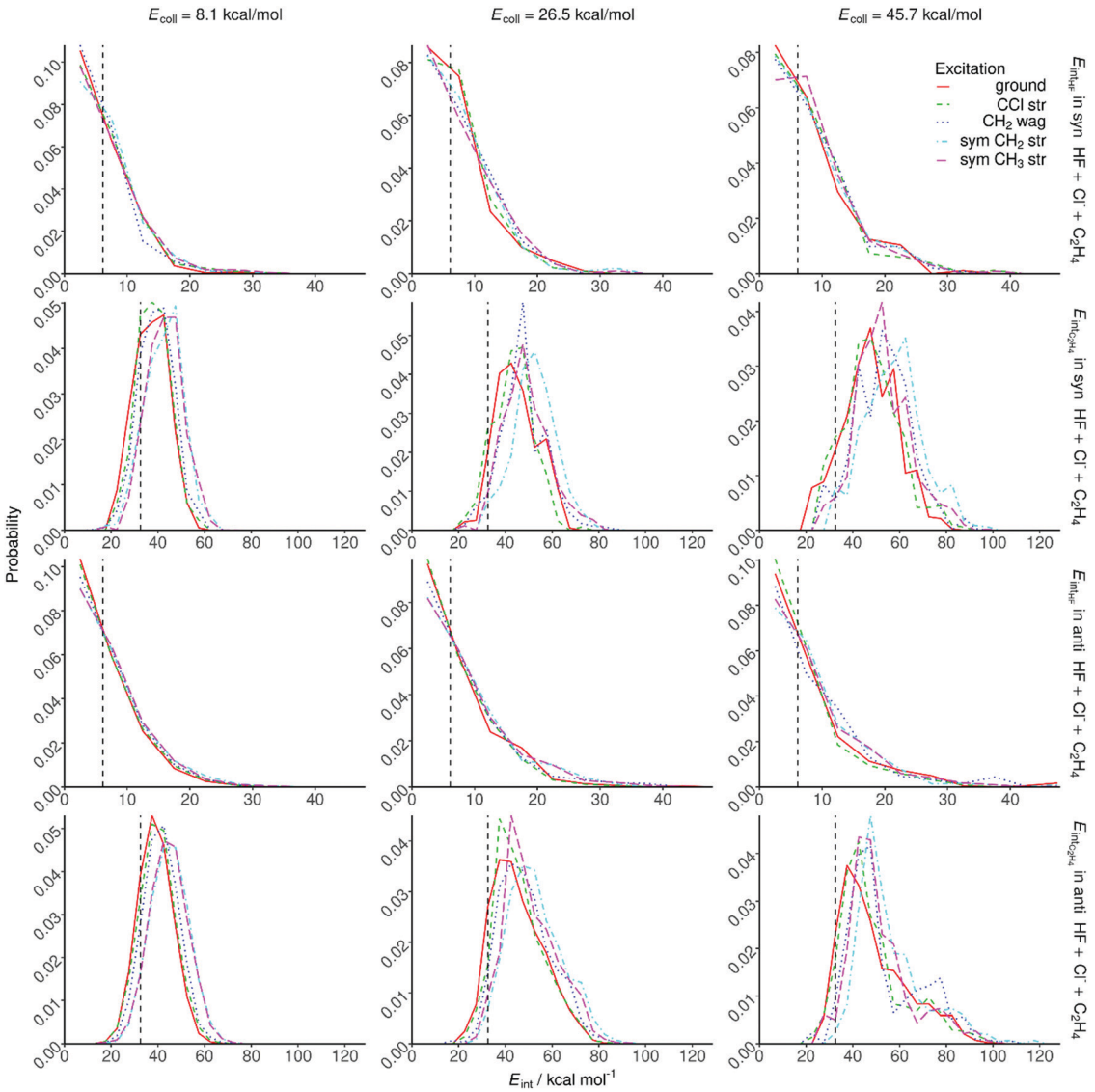

Fig. 10 Normalized product internal energy distributions for the F^- + $CH_3CH_2Cl(v_k = 0, 1)$ [k = 10, 7, 1, 3] *syn*- and *anti*-E2 reactions at different collision energies. Vertical dashed lines indicate the ZPE of the products.

shown for selected modes in Fig. 13 and 14. However, for the symmetric CH_3 stretching mode the standard HB provides unphysically high vibrational excitations up to 20 quanta as shown in Fig. 13. This is due to the failure of the normal mode analysis caused by internal rotation of the CH_3 group as already discussed for the IVR analysis of the CH_3CH_2Cl reactant. The 1GB approach solves this issue by assigning nearly zero weights for the unphysical states, thereby providing realistic vibrational populations for the symmetric CH_3 stretching mode as also shown in Fig. 13. We note that we have tested different Gaussian widths (δ values) as shown in Fig. S3 (ESI†). As δ decreases the unphysical populations tend to vanish while the statistical uncertainty increases. Since the results with δ = 0.2 and 0.1 become very similar, we use the statistically more robust δ = 0.2 in this study.

According to the 1GB results shown in Fig. 13 and 14, the CH_2 and CH_3 stretching modes are mainly in vibrational ground state (80–90%) and 10–20% one-quantum excitations are seen. Upon CH_2/CH_3 initial stretching excitations the corresponding product modes are not found significantly more excited, as a signature of strong IVR. For the CF stretching and CH_2 wagging modes significantly more excitations are obtained up to about 4 quanta (Fig. 14), as expected, because these modes couple with the reaction coordinate the most efficiently. We also see some translational and vibrational energy transfer into these modes, in accord with the internal energy distributions. Unlike for the symmetric CH_3 stretching, for the CF and CH_2 stretching as well as CH_2 wagging modes HB provides similar vibrational distributions with only slightly higher excitations and better statistics as 1GB, as shown in Fig. S4 (ESI†).

For the C_2H_4 products, where internal rotation is not a concern, we apply HB and give the mode-specific vibrational distributions in Fig. S5–S7 (see ESI†) for the $FH\cdots Cl^-$ + C_2H_4,

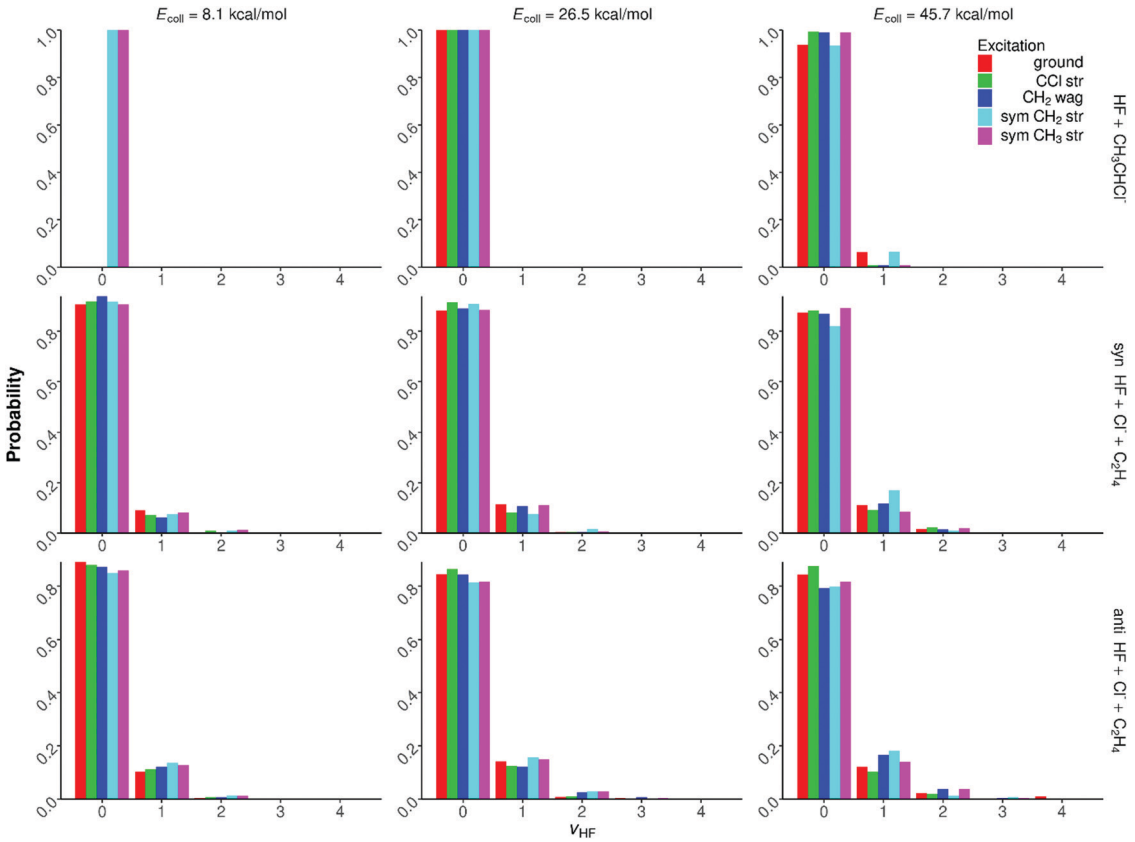

Fig. 11 Normalized HF vibrational distributions for the F^- + $CH_3CH_2Cl(v_k = 0, 1)$ [k = 10, 7, 1, 3] → HF + CH_3CHCl^-, *syn*-E2, and *anti*-E2 reactions at different collision energies.

syn-E2, and *anti*-E2 channels, respectively. Here we consider different CH_2 wagging and stretching modes and the results and conclusions are similar to the above-discussed findings for the CH_3CH_2F product of the S_N2 channel.

IV. Summary and conclusions

Following our recent join theoretical–experimental study[48] on the dynamics of the F^- + $CH_3CH_2Cl(v = 0)$ S_N2 and E2 processes, we have carried out mode-specific QCT computations for the C–Cl stretching, CH_2 wagging, CH_2 stretching, and CH_3 stretching excited F^- + $CH_3CH_2Cl(v_k = 1)$ [k = 10, 7, 1, 3] reactions using our full-dimensional analytical high-level PES.[48] The most important results and conclusions of the present study can be summarized as follows:

(a) The analytical PES usually reproduces the all-electron CCSD(T)/complete-basis-set-quality benchmark[47,60] stationary-point relative energies within a few tenths of a kcal mol^{-1}.

(b) IVR prior to collision is significant, nevertheless, some mode specificity is maintained.

(c) Normal mode analysis for the symmetric CH_3 stretching mode of the CH_3CH_2Cl and CH_3CH_2F molecules fails due to the internal rotation of the methyl group, which issue can be treated by using the 1GB method[49–51] for mode-specific polyatomic product vibrational analysis.

(d) The *syn*- and *anti*-E2 pathways can be almost unambiguously separated numerically based on the Cl–C_α–C_β–F dihedral angles at the E2 transition states.

(e) C-Cl stretching excitation enhances the S_N2 channel, proton abstraction occurs from the alpha carbon and enhanced by CH_2 stretching excitation, and the $FH\cdots Cl^-$ + C_2H_4 and E2 channels proceed with beta proton transfer and are enhanced by both CH_2 and CH_3 stretching excitations due to IVR.

(f) *Anti*-E2 is kinetically preferred and thus dominates over *syn*-E2. Furthermore, *anti*-E2 has even higher reactivity than the thermodynamically favored S_N2, due to the wider reactive attack angle range for the former as also proposed in ref. 48.

(g) Double-inversion and front-side attack S_N2 pathways and induced inversion of the reactant are minor with only about 0.1% probability for the title reaction.

(h) As collision energy increases and the reactions become direct, scattering angle distributions show backward dominance for S_N2 and forward preference for $FH\cdots Cl^-$ complex formation and E2. For the proton-abstraction channel forward scattering is found indicating significant direct stripping mechanism.

(i) Attack angle distributions show that the direct S_N2, $FH\cdots Cl^-$ complex-forming, *syn*-E2, and *anti*-E2 channels favor initial back-side, side-on, front-side, and back-side attack, respectively.

(j) The S_N2 channel produce internally hot CH_3CH_2F molecules, where mainly the CF stretching and CH_2 wagging modes

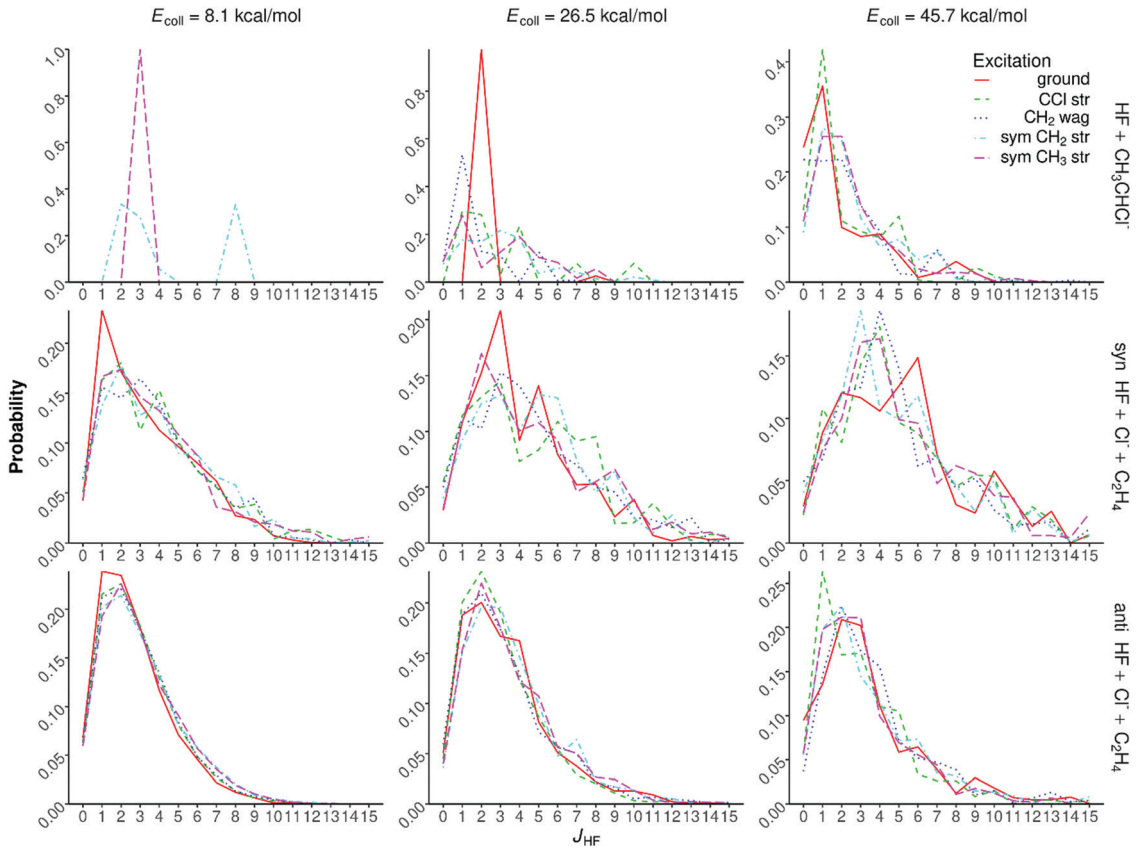

Fig. 12 Normalized HF rotational distributions for the F^- + $CH_3CH_2Cl(v_k = 0, 1)$ [k = 10, 7, 1, 3] → HF + CH_3CHCl^-, *syn*-E2, and *anti*-E2 reactions at different collision energies.

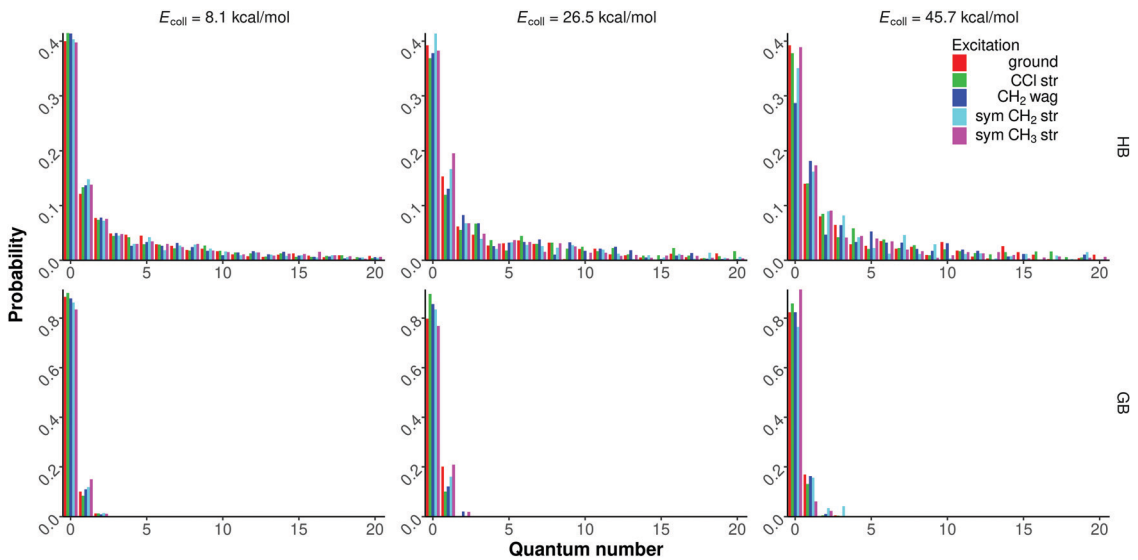

Fig. 13 Normalized symmetric CH_3 stretching mode specific vibrational distributions for the CH_3CH_2F product of the F^- + $CH_3CH_2Cl(v_k = 0, 1)$ [k = 10, 7, 1, 3] S_N2 reactions at different collision energies obtained with histogram binning (HB) and Gaussian binning (GB).

are excited. Initial CH_2/CH_3 stretching excitation energy transfers into the internal energy of the CH_3CH_2F S_N2 and C_2H_4 E2 products.

(k) A significant fraction of the $FH\cdots Cl^-$ complexes are in a Feshbach-type resonance state with higher internal energies than the dissociation energy of the complex.

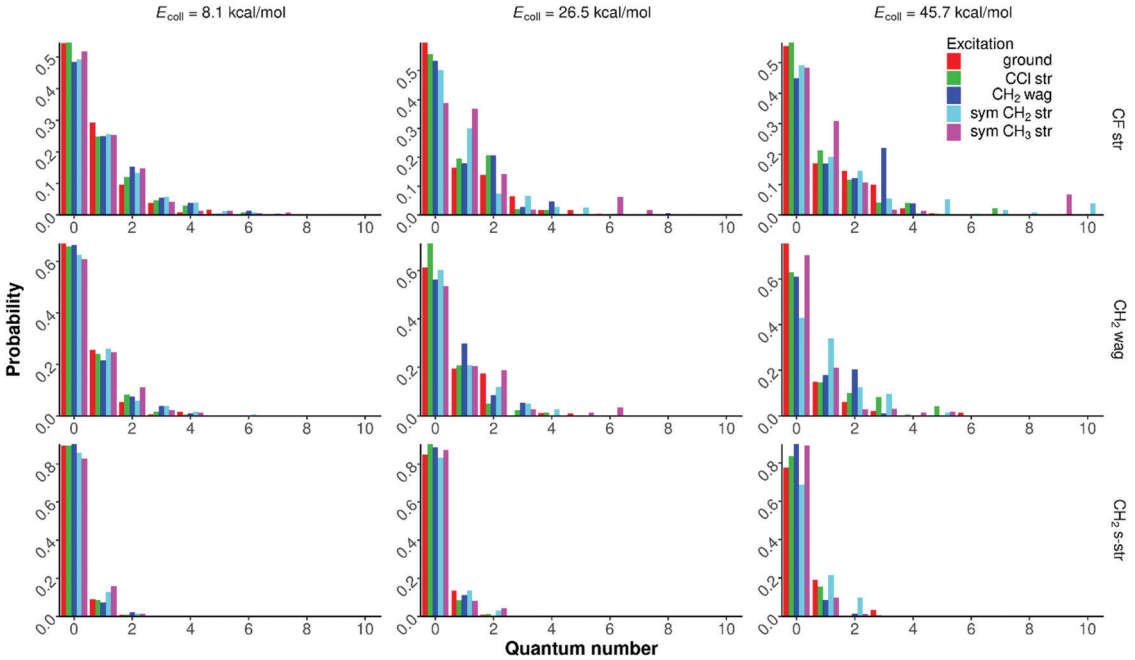

Fig. 14 Normalized CF stretching, CH_2 wagging, and symmetric CH_2 stretching mode specific vibrational distributions for the CH_3CH_2F product of the F^- + $CH_3CH_2Cl(v_k = 0, 1)$ [k = 10, 7, 1, 3] S_N2 reactions at different collision energies obtained with Gaussian binning.

(l) HF products are vibrationally and rotationally cold, especially for the proton abstraction channel. The HF products have significantly higher rotational excitations *via* the *syn*-E2 channel than *anti*-E2.

(m) Standard histogram binning provides significant populations for energetically forbidden CH_3 stretching vibrational states of CH_3CH_2F, whereas the 1GB method assigns nearly zero weights for these unphysical states and gives realistic cold distributions. Histogram binning performs well for mode-specific vibrational analysis of C_2H_4, which is not affected by internal rotations.

The present study and the above results show the current state-of-the-art of polyatomic reaction dynamics for a 9-atomic system. We hope that the techniques used in this study may be utilized in future similar theoretical investigations. The timescale of IVR may hinder mode-specific experimental studies for the title reaction; nevertheless, we hope that the present findings may motivate future measurements of vibrational effects on the dynamics of ion–molecule reactions.

Conflicts of interest

There are no conflicts of interest to declare.

Acknowledgements

We thank the financial support of the National Research, Development and Innovation Office – NKFIH (K-125317); the Ministry of Human Capacities, Hungary (20391-3/2018/FEKUSTRAT); Project no. TKP2021-NVA-19, provided by the Ministry of Innovation and Technology of Hungary from the National Research, Development and Innovation Fund, financed under the TKP2021-NVA funding scheme; and the Momentum (Lendület) Program of the Hungarian Academy of Sciences. Furthermore, we acknowledge KIFÜ for awarding us access to computational resource based in Hungary at Debrecen.

References

1 G. C. Schatz, M. C. Colton and J. L. Grant, *J. Phys. Chem.*, 1984, **88**, 2971.
2 A. Sinha, M. C. Hsiao and F. F. Crim, *J. Chem. Phys.*, 1990, **92**, 6333.
3 M. J. Bronikowski, W. R. Simpson, B. Girard and R. N. Zare, *J. Chem. Phys.*, 1991, **95**, 8647.
4 D. H. Zhang and J. C. Light, *J. Chem. Soc., Faraday Trans.*, 1997, **93**, 691.
5 S. Yoon, S. Henton, A. N. Zivkovic and F. F. Crim, *J. Chem. Phys.*, 2002, **116**, 10744.
6 C. Murray and A. J. Orr-Ewing, *Int. Rev. Phys. Chem.*, 2004, **23**, 435.
7 S. Yan, Y. Wu, B. Zhang, X.-F. Yue and K. Liu, *Science*, 2007, **316**, 1723.
8 W. Zhang, H. Kawamata and K. Liu, *Science*, 2009, **325**, 303.
9 J. Li, B. Jiang and H. Guo, *J. Am. Chem. Soc.*, 2013, **135**, 982.
10 B. Jiang and H. Guo, *J. Am. Chem. Soc.*, 2013, **135**, 15251.
11 W. Yan, F. Meng and D. Y. Wang, *J. Phys. Chem. A*, 2013, **117**, 12236.
12 J. Espinosa-Garcia, *J. Phys. Chem. A*, 2014, **118**, 3572.
13 R. Welsch and U. Manthe, *J. Chem. Phys.*, 2014, **141**, 051102.
14 G. Czakó and J. M. Bowman, *J. Phys. Chem. A*, 2014, **118**, 2839.

15 J. Qi, H. Song, M. Yang, J. Palma, U. Manthe and H. Guo, *J. Chem. Phys.*, 2016, **144**, 171101.
16 B. Fu, X. Shan, D. H. Zhang and D. C. Clary, *Chem. Soc. Rev.*, 2017, **46**, 7625.
17 D. Zhang, J. Yang, Z. Chen, R. Chen, B. Jiang, D. Dai, G. Wu, D. Zhang and X. Yang, *Phys. Chem. Chem. Phys.*, 2017, **19**, 13070.
18 D. Lu and J. Li, *Theor. Chem. Acc.*, 2020, **139**, 157.
19 D. Lu, J. Li and H. Guo, *CCS Chem.*, 2020, **2**, 882.
20 D. Papp, J. Li, H. Guo and G. Czakó, *J. Chem. Phys.*, 2021, **155**, 114303.
21 D. Gao and D. Wang, *Phys. Chem. Chem. Phys.*, 2021, **23**, 26911.
22 A. Marjollet, L. Inhester and R. Welsch, *J. Chem. Phys.*, 2022, **156**, 044101.
23 H. Song, W. Xie, C. Zhang and M. Yang, *J. Phys. Chem. A*, 2022, **126**, 663.
24 S. R. Vande Linde and W. L. Hase, *J. Am. Chem. Soc.*, 1989, **111**, 2349.
25 P. Ayotte, J. Kim, J. A. Kelley, S. B. Nielsen and M. A. Johnson, *J. Am. Chem. Soc.*, 1999, **121**, 6950.
26 S. Schmatz, *ChemPhysChem*, 2004, **5**, 600.
27 C. Hennig and S. Schmatz, *J. Chem. Phys.*, 2004, **121**, 220.
28 C. Hennig and S. Schmatz, *J. Chem. Phys.*, 2005, **122**, 234307.
29 C. Hennig and S. Schmatz, *Chem. Phys. Lett.*, 2007, **446**, 250.
30 M. Kowalewski, J. Mikosch, R. Wester and R. de Vivie-Riedle, *J. Phys. Chem. A*, 2014, **118**, 4661.
31 Y. Wang, H. Song, I. Szabó, G. Czakó, H. Guo and M. Yang, *J. Phys. Chem. Lett.*, 2016, **7**, 3322.
32 I. Szabó and G. Czakó, *J. Chem. Phys.*, 2016, **145**, 134303.
33 Y. Li, Y. Wang and D. Wang, *J. Phys. Chem. A*, 2017, **121**, 2773.
34 M. Stei, E. Carrascosa, A. Dörfler, J. Meyer, B. Olasz, G. Czakó, A. Li, H. Guo and R. Wester, *Sci. Adv.*, 2018, **4**, eaas9544.
35 B. Olasz and G. Czakó, *J. Phys. Chem. A*, 2018, **122**, 8143.
36 T. Michaelsen, B. Bastian, P. Strübin, J. Meyer and R. Wester, *Phys. Chem. Chem. Phys.*, 2020, **22**, 12382.
37 M. Pan, H. Xiang, Y. Li and H. Song, *Phys. Chem. Chem. Phys.*, 2021, **23**, 17848.
38 A. A. Viggiano, R. A. Morris, J. S. Paschkewitz and J. F. Paulson, *J. Am. Chem. Soc.*, 1992, **114**, 10477.
39 D. S. Tonner and T. B. McMahon, *J. Am. Chem. Soc.*, 2000, **122**, 8783.
40 F. M. Bickelhaupt, E. J. Baerends, N. M. M. Nibbering and T. Ziegler, *J. Am. Chem. Soc.*, 1993, **115**, 9160.
41 A. P. Bento, M. Solà and F. M. Bickelhaupt, *J. Chem. Theory Comput.*, 2008, **4**, 929.
42 X.-P. Wu, X.-M. Sun, X.-G. Wei, Y. Ren, N.-B. Wong and W.-K. Li, *J. Chem. Theory Comput.*, 2009, **5**, 1597.
43 L. Yang, J. Zhang, J. Xie, X. Ma, L. Zhang, C. Zhao and W. L. Hase, *J. Phys. Chem. A*, 2017, **121**, 1078.
44 E. Carrascosa, J. Meyer, J. Zhang, M. Stei, T. Michaelsen, W. L. Hase, L. Yang and R. Wester, *Nat. Commun.*, 2017, **8**, 25.
45 M. Mugnai, G. Cardini and V. Schettino, *J. Phys. Chem. A*, 2003, **107**, 2540.
46 B. Ensing and M. L. Klein, *Proc. Natl. Acad. Sci. U. S. A.*, 2005, **102**, 6755.
47 V. Tajti and G. Czakó, *J. Phys. Chem. A*, 2017, **121**, 2847.
48 J. Meyer, V. Tajti, E. Carrascosa, T. Győri, M. Stei, T. Michaelsen, B. Bastian, G. Czakó and R. Wester, *Nat. Chem.*, 2021, **13**, 977.
49 G. Czakó and J. M. Bowman, *J. Chem. Phys.*, 2009, **131**, 244302.
50 L. Bonnet and J. Espinosa-García, *J. Chem. Phys.*, 2010, **133**, 164108.
51 G. Czakó, *J. Phys. Chem. A*, 2012, **116**, 7467.
52 T. Győri and G. Czakó, *J. Chem. Theory Comput.*, 2020, **16**, 51.
53 W. L. Hase, *Encyclopedia of Computational Chemistry*, Wiley, New York, 1998, pp. 399–407.
54 G. Czakó, B. C. Shepler, B. J. Braams and J. M. Bowman, *J. Chem. Phys.*, 2009, **130**, 084301.
55 P. Papp, V. Tajti and G. Czakó, *Chem. Phys. Lett.*, 2020, **755**, 137780.
56 I. Szabó and G. Czakó, *Nat. Commun.*, 2015, **6**, 5972.
57 V. Tajti, T. Győri and G. Czakó, *J. Chem. Phys.*, 2021, **155**, 124301.
58 A. Y. Dymarsky and K. N. Kudin, *J. Chem. Phys.*, 2005, **122**, 124103.
59 K. N. Kudin and A. Y. Dymarsky, *J. Chem. Phys.*, 2005, **122**, 224105.
60 G. Czakó, T. Győri, B. Olasz, D. Papp, I. Szabó, V. Tajti and D. A. Tasi, *Phys. Chem. Chem. Phys.*, 2020, **22**, 4298.
61 M. L. Weichman, J. A. DeVine, M. C. Babin, J. Li, L. Guo, J. Ma, H. Guo and D. M. Neumark, *Nat. Chem.*, 2017, **9**, 950.